



Photo-mineralization of noxious *o*-toluidine water pollutant by nano-ZnO: The role of the oxide surface texture on the kinetic path

V. Pifferi^{a,*}, G. Cappelletti^{a,**}, S. Ardizzone^a, L. Falciola^a, C. Di Bari^{a,1}, F. Spadavecchia^{a,2}, D. Meroni^a, A. Carrà^{a,3}, G. Cerrato^b, S. Morandi^b, E. Davoli^c

^a Dipartimento di Chimica, Università degli Studi di Milano, via Golgi 19, 20133 Milano, Italy

^b Dipartimento di Chimica & NIS Interdept. Centre, Università degli Studi di Torino, Via P. Giuria 7, 10125 Torino, Italy

^c IRCCS Istituto Mario Negri, Via La Masa 19, 20156 Milano, Italy

ARTICLE INFO

Article history:

Received 17 June 2014

Received in revised form 22 August 2014

Accepted 26 August 2014

Available online 3 September 2014

Keywords:

ZnO nanoparticles

o-Toluidine

Photodegradation

LC/MS

Kinetic paths.

ABSTRACT

Highly toxic *o*-toluidine pollutant was photo-degraded in water by using ZnO nanoparticles. The tested powders were both commercial and laboratory-made, the latter obtained by means of two innovative synthetic procedures. The disappearance and the relative mineralization of the molecule were followed by HPLC/UV and TOC determinations, respectively. Intermediate products were identified by coupling LC/MS of the eluate after 3 h of reaction and ATR-FTIR analyses of the used ZnO powders at the end of photocatalytic tests. Selected degradation paths, characterized by different kinetic degradation rates, can be suggested as a function of the different surface texture, the effective photocatalytic active area and the e^-/h^+ recombination processes of the ZnO particles.

© 2014 Elsevier B.V. All rights reserved.

1. Introduction

o-Toluidine is an aromatic amine that is widely used in the fabrication of azo-dyes, in the rubber industry, and pharmaceutical production [1,2]. However, it is genotoxic and carcinogenic and therefore it should be regarded as potentially toxic to reproduction, according to EU Technical Guidance Document. Short-term exposure to this compound may induce methaemoglobinemia, whereas long-term or repeated exposure could be carcinogenic to humans [3], particularly inducing bladder cancer [4]. The general population may be exposed to low concentrations [5] of *o*-toluidine in indoor and outdoor surroundings such as air, tobacco smoke, or food, or by dermal contact with commercial products.

Since it is also bio-refractory, novel degradation processes have to be explored. In this context, advanced oxidation processes (AOPs), which combine ozone, UV, hydrogen peroxide, and/or

catalyst, generating extremely oxidant hydroxyl radicals, offer a powerful water treatment solution. Fenton [6], electro-Fenton [7], and photo-Fenton [8] processes, or a combination of them, have been proposed in the recent literature for the degradation of *o*-toluidine. The only literature work focused on the degradation of *o*-toluidine in the gas phase by heterogeneous photocatalysis is reported by An *et al.* [9], who used TiO₂ thin films and UV irradiation. They achieved a degradation efficiency of 98.7% (*o*-toluidine concentration of about 4.5 ppm, illumination of 240 min), focusing the attention on the possible degradation paths.

Zinc oxide, beside its traditional application fields (cosmetic materials, coatings, pharmaceutical, piezoelectric devices), has recently attracted more attention in photocatalysis for the degradation of organic and inorganic pollutants in both aqueous and gas media [10–12]. Indeed, ZnO, due to its oxidation power under UV irradiation (band gap of 3.37 eV), can be considered one of the best photocatalytic semiconductors, second only to TiO₂. Comparison of the two semiconductors (e.g. band-edge positions) is reported elsewhere [13].

The photocatalytic properties of ZnO are directly dependent on many physicochemical factors such as morphological, structural, and optical properties. Consequently, studies on the synthesis, characterization, and properties of nanosized ZnO have received significant attention in the recent years [10–12]. Different techniques for preparing ZnO nanoparticles have been investigated such as sol–gel processes, chemical coprecipitation, chemical vapor

* Corresponding author. Tel.: +39 0 250314222.

** Corresponding author. Tel.: +39 0 250314228; fax: +390250314228.

E-mail addresses: valentina.pifferi@unimi.it (V. Pifferi),

giuseppe.cappelletti@unimi.it (G. Cappelletti).

¹ Present address: Instituto de Catalisis y Petroleoquímica, Consejo Superior de Investigaciones Científicas, C/Marie Curie 2, L10, 28049 Madrid, Spain.

² Present address: Eni S.p.A. - Refining & Marketing Division, San Donato Milanese Research Center, Via F. Maritano 26, I-20097 San Donato Milanese, MI, Italy.

³ Present address: Saes Getters - Viale Italia 77, I-20020 Lainate, MI, Italy.

deposition, thermal decomposition, hydrothermal synthesis, spray pyrolysis, and microemulsion precipitation [14–16].

On the basis of the present considerations, in this work, *o*-toluidine was chosen as a model substrate to be photocatalytically degraded in water by ZnO nanopowders. To the authors' best knowledge, no previous studies on this topic can be found in the literature. Three different ZnO samples were considered: a commercial one (by Aldrich, labeled Z.comm) and two homemade nano-powders synthesized by a simple sol–gel route modified from the literature (Z.SG) [17] and by a newly developed microemulsion route (Z.ME). Since the size of the microemulsion is typically smaller than 100 nm [18,19], it can be viewed as nano-reactor for ZnO synthesis. Such a method allows the control over particle size and morphology by adjusting the composition of the microemulsion and the type of surfactant [18,20,21].

Moreover, most of literature studies have focused on the genotoxicity of *o*-toluidine and its co-mutagenic action with β -carboline [22]. Its degradation intermediates produced are instead scantily investigated [23], although they might represent highly toxic and recalcitrant compounds themselves. Here, the formation of undesired degradation byproducts was studied in detail by HPLC/MS analyses together with the role played by the oxide surface texture in affecting the *o*-toluidine degradation mechanism.

2. Experimental

All chemicals were of reagent grade purity and were used without further purification; doubly distilled water passed through a Milli-Q apparatus was used to prepare solutions and suspensions.

Three different kinds of ZnO nanoparticles were used as photocatalysts in order to degrade the *o*-toluidine pollutant: a commercial one (Z.comm) and two laboratory-made samples synthesized by both traditional sol–gel (Z.SG) and a newly developed microemulsion (Z.ME) route.

2.1. Synthesis via sol–gel (Z.SG)

A modified sol–gel method was adopted from the literature [17].

ZnO nanoparticles were prepared in ethanol medium by the reaction of zinc acetate and sodium hydroxide. 3.80 g of $\text{Zn}(\text{CH}_3\text{COO})_2 \cdot 2\text{H}_2\text{O}$ was dissolved in 240 mL of ethanol using vigorous magnetic stirring (300 rpm) at 80 °C for 30 min followed by cooling in ice water for 5 min. Keeping the solution in ice water, a 0.5 M NaOH aqueous solution (78 mL) was slowly added while stirring. The mixture was continuously stirred for 24 h: it slowly turned into a gel and finally in a whitish colloidal solution. A white precipitate was separated by centrifugation and repeatedly washed using a mixture of ethanol and *n*-heptane (3:1 volume ratio). Then, it was dried in oven at 90 °C and subsequently calcined at 400 °C for 6 h under O_2 stream (9 nL/h).

2.2. Synthesis via inverse microemulsion (Z.ME)

LUTENSOL A4N surfactant (non-ionic alkylpolyethylene glycol, HLB ca. 9, cloud point ca. 62 °C, molar mass 370 g mol⁻¹) by BASF was chosen as emulsifying agent. 2.8 mL of the present surfactant was dissolved in 17 mL of *n*-heptane. After stirring for about 30 min at 50 °C, 1-hexanol (16.3 g) was added as co-surfactant. The mixture was kept under stirring at room temperature for another 30 min. Then 3.5 mL of NH_4OH diluted in 22 mL of water was slowly added. After 90 min stirring, $\text{Zn}(\text{NO}_3)_2 \cdot 6\text{H}_2\text{O}$ (8.9 g), previously dissolved in 15.5 mL of ethanol, was added drop-wise into the transparent microemulsion. The resulting precursor-containing mixture turned into a milky-white suspension and was stirred overnight. Then, the precipitate was recovered by filtration and washed several times with ethanol. The residual wet solid was dried in oven at

90 °C and subsequently calcined at 400 °C for 6 h under O_2 stream (9 nL/h).

2.3. Sample characterization

The BET surface area and BJH pore size and distribution of the powders were determined from nitrogen adsorption–desorption isotherms at 77 K (Coulter SA 3100 apparatus).

Room-temperature X-ray powder diffraction (XRPD) patterns were collected between 20 and 80° (2 θ range, $\Delta 2\theta = 0.1^\circ$, $t = 6$ s) with a Siemens D500 diffractometer, using Cu K α radiation.

Particles morphology was obtained by high-resolution transmission electron microscopy (HR-TEM), using a JEOL JEM 3010UHR (300 kV) microscope fitted with a LaB₆ single-crystal filament and an Oxford INCA Energy TEM 200 energy-dispersive X-ray (EDX) detector. All samples were dry deposited on Cu “holey” carbon grids (200 mesh).

The particle populations ($\langle d \rangle^{\text{GRAN}}$) of the ZnO samples were analyzed by a Beckman Coulter N4 analyzer. The instrument determines particle/aggregate size by photon correlation spectroscopy (PCS).

Diffuse reflectance spectra (DRS) of the powders were measured on a UV–Vis scanning spectrophotometer (Perkin-Elmer, Lambda 35) equipped with a diffuse reflectance accessory. A “total white” Perkin-Elmer reference material was used as reference.

FTIR spectra (128 scans, 4 cm⁻¹ resolution) were collected on a Bruker IFS 66 spectrometer, equipped with an MCT detector. Samples were pressed into self-supporting pellets (approx. 10–15 mg cm⁻²) and placed in a quartz cell fitted with KBr windows. Prior to any FTIR measurements, all samples were activated in vacuo at either room temperature (RT) or 250 °C, connecting the quartz cell to a conventional high-vacuum glass line capable of a residual pressure <10⁻⁴ Torr.

Photocurrent measurements were performed by using ZnO thin films prepared by spin-coating a 2-ethanol suspension of the oxide powder with a Spin150 spin-coater (SPS, ATP GmbH, 2000 rpm for 20 s, eight layers) onto fluorine-doped tin oxide (FTO) conducting glass (Aldrich, 2.3 mm thick, $\sim 7 \Omega/\text{sq}$ surface resistivity). The as-prepared films were finally sintered at 400 °C in air for 1 h. The photocurrent developed by irradiating the ZnO photoanode with UV light (see Section 2.4) was recorded by a microIII Autolab potentiostat/galvanostat (EcoChemie, The Netherlands) [24]. The dark/light alternation was repeated for at least six times, in order to obtain reproducible transient patterns. The photoelectrochemical cell was a three-compartment one, with two counter-electrodes, both consisting of a Pt wire parallel to the working electrode, a saturated calomel electrode as reference, a Luggin capillary in order to minimize the ohmic drop, and a ZnO film located in the middle of the cell as working electrode [24]. All the measurements were carried out in N_2 atmosphere, after degassing the cell with nitrogen flow for at least 10 min. Preliminary linear sweep voltammetries (LSV) were recorded in the same experimental conditions at a scan rate of 50 mV s⁻¹ in order to evaluate the potential at which the photocurrent is constant to be chosen as working potential for the chronoamperometric tests (1.0 V SCE).

2.4. Photocatalytic setup

All degradation tests were carried out at spontaneous pH and at 25 °C, in a 500 mL cylindrical jacketed glass reactor. *o*-Toluidine (purity > 99%), used as the target compound, was purchased from Sigma-Aldrich. The optimal conditions for the photocatalytic tests were the following: initial pollutant concentration 25 ppm and photocatalyst concentration 0.3 g L⁻¹.

The mineralization degree of *o*-toluidine was determined by TOC analyses (TOC-VCN Shimadzu total organic carbon analyzer) and its removal was confirmed by HPLC measurements.

Aliquots of raw reaction media were analyzed by performing an isocratic separation with an HPLC/UV system (Agilent Technologies 1200 Series). Elution was carried out by using a normalbore RP-column (Eclipse XDB-C18) with a mobile phase consisting of methanol and water in a ratio 70:30. Memory effect was controlled and monitored by injecting blank samples during analysis. *o*-Toluidine and its degradation products were revealed by using an on-line UV Diode Array Detector (DAD, G1315-D) set at 230 nm.

In order to investigate the photo-degradation mechanism of *o*-toluidine, aliquots of raw reaction media were examined also by using heart cutting chromatographic approach [25,26], that consists of consecutive LC/MS analyses. A triple quadrupole mass spectrometer ESI/QqQ (API3000-AB Sciex) coupled to the microbore-HPLC system was employed to recognize *o*-toluidine degradation products. Nano-ESI/FTMS (LTQ/Orbitrap - Thermo Scientific), high resolution, mass analyzer was also used whenever the ion-suppression effect was found critical for QqQ-detection. This methodology was used only as a backup solution, avoiding the well-known micro-fluidics criticisms [27,28]. Further, attenuated total reflectance Fourier transform infrared spectroscopy (ATR-FTIR; Jasco 4200) analyses were carried out on used ZnO powders at the end of the reaction (after 360 min) to corroborate the LC/MS evidences.

Photolysis and photocatalytic tests were performed under UV-A irradiation, using a 500 W iron halogenide lamp (Jelosil, model HG 500) emitting in the 315–400 nm wavelength range and presenting an effective power density of 75 mW cm^{-2} (measured by Thorlabs). The position of the lamp (15 cm from the reactor) was selected so as to produce an irradiated area covering the whole reactor. *o*-Toluidine was allowed to reach adsorption-desorption equilibrium after 20 min in dark conditions. Dark tests performed for 6 h—a period equal to the photoreaction time—showed a pollutant adsorption <20% for all the tested samples. Direct photolysis under UV irradiation was negligible.

Photocatalytic tests on selected samples were performed also under simulated solar irradiation (halogen lamp by Lot Oriel, effective power density 1 mW cm^{-2} in the range 280–400 nm and 14 mW cm^{-2} in the range 400–800 nm).

3. Results and discussion

3.1. Photocatalytic experiments

HPLC/UV measurements were used to evaluate the *o*-toluidine disappearance during the photocatalytic experiment performed in ZnO slurries, by using both commercial (Z.comm) and laboratory-made (Z.SG and Z.ME) nanopowders. In order to quantify the residual amount of *o*-toluidine in raw reaction medium, the chromatographic apparatus was calibrated by injecting a series of standard *o*-toluidine solution ($t_R = 14.5 \text{ min}$). The calibration plot is reported in Fig. S1, confirming a good linearity ($R^2 = 0.990$), a good sensitivity in the low-concentration range (slope $19.1 \pm 0.5 \text{ mAU s ppm}^{-1}$) and a limit of detection close to 20 ng injected. Moreover, the superior chromatographic capacity of this methodology allows us to obtain eluates suitable for ensuing LC/MS byproduct characterizations.

Fig. 1 shows the % degradation of *o*-toluidine as a function of reaction time for the three tested samples. The photodegradation trends show that the best efficiency is achieved by the commercial Z.comm, which reaches a quasi-plateau region at the end of the reaction time (83%, Table 1, 2nd column); the homemade powders, instead, lead to a lower % removal (Table 1, 2nd column),

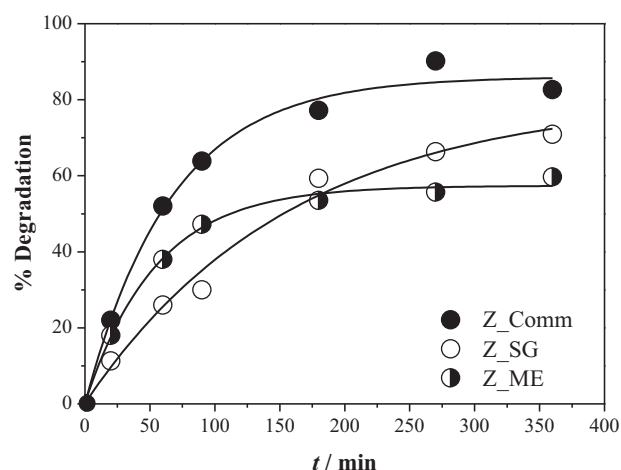


Fig. 1. % HPLC disappearance of *o*-toluidine (25 ppm) by using Z.comm, Z.SG, and Z.ME, fitted by pseudo-first-order exponential equations.

Table 1

% of degradation (HPLC) at 360 min and relative kinetic constants at 90 min, % of mineralization (TOC) at 360 min for each tested sample.

Sample	% HPLC ($t = 360 \text{ min}$)	$k_{90}^{\text{HPLC}} \times 10^3$ (min^{-1})	% TOC ($t = 360 \text{ min}$)
Z.comm	83	11.6 ± 0.3	26
Z.SG	71	4.3 ± 0.3	15
Z.ME	60	7.2 ± 0.4	12

especially in the case of the sample synthesized by microemulsion route (Z.ME). Particularly, while Z.ME reaches a quasi-plateau at degradation values lower than Z.comm, the *o*-toluidine disappearance by Z.SG photocatalyst seems not to reach an asymptotic value after 360 min reaction time.

In order to produce a significant comparison among the present samples, experimental data from HPLC/UV, relative to the first 90 min of reaction time, were elaborated on the grounds of a pseudo-first-order kinetic law. The experimental points are interpolated by linear regressions with high correlation coefficients (Fig. S2). The rate constants (Table 1, 3th column) show that the best photocatalytic sample is again the Z.comm, according to the final % HPLC degradation, while the microemulsion synthesized sample (Z.ME) seems to be more efficient with respect to the sol-gel one (Z.SG) in the first 90 min reaction time. Although a significant disappearance of the pollutant was observed for all samples, a relevant final mineralization was not achieved (Table 1, 4th column), showing that accumulation of stable intermediates is possibly taking place.

Then, Z.comm, showing the best UV photocatalytic degradation/mineralization of *o*-toluidine, was tested photocatalytically under simulated solar irradiation, even if the sample is not promoted for visible activity. Fig. 2 shows the difference percentage in performance passing from UV to solar light in terms of HPLC removal/TOC mineralization as a function of reaction time. As expected, both the removal and mineralization are depressed in the case of solar irradiation (table in inset in Fig. 2); actually, the gap between UV/solar efficiency increases at increasing the reaction time. Notwithstanding the low activity in the visible region, these results are very promising since no promotion strategy was adopted to extend the photoactivity of the ZnO samples in the visible; however, further studies are necessary to increase the degradation efficiency under solar irradiation especially by addition of host dopant species that could expand the light absorption in the visible region [29–31].

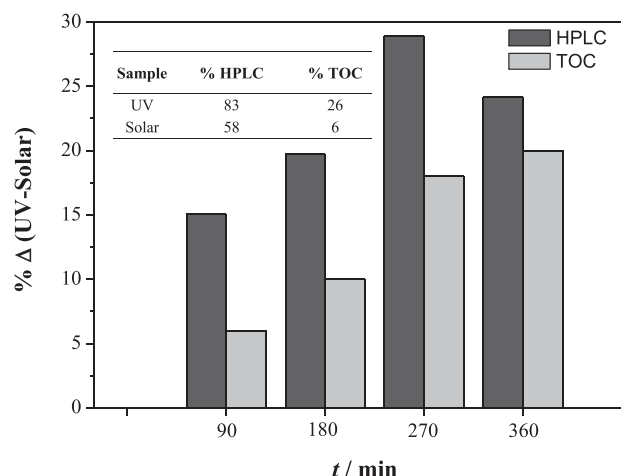


Fig. 2. Comparison of photocatalytic performances of Z.comm in terms of difference percentage of HPLC removal/TOC mineralization passing from UV to solar light as a function of reaction time. Inset data at the end of the photocatalytic treatment (360 min).

The above-reported findings show in any case (UV/solar) the discrepancy between *o*-toluidine removal and its final mineralization, suggesting the occurrence of a complex kinetic pattern, which necessarily implies surface reaction steps. A more complete picture of the possible byproducts can be drawn in the case of UV irradiation, which leads to the progressive appearance of appreciable amounts of possible degraded species.

Table 2

LC/MS intermediates: NO₂-Tol = *o*-nitrotoluene; CH₃-Ph = *o*-methylphenol; OH-BzH = 2-hydroxybenzaldehyde (+++ = most abundant, ++ = abundant, + = relevant, o = appreciable, t = traces).

Intermediates	m/z	Z.comm		Z.SG		Z.ME	
		3 h	6 h	3 h	6 h	3 h	6 h
NO ₂ -Tol ⁺	138	+++	+	++	+/o	++	+
CH ₃ -Ph	109	o	t	—	—	—	—
OH-BzH	123	+	+	t	t	t	t

All species have been revealed as proton adducts, [M+H]⁺.

⁺ Data acquired with nano-ESI/FTMS (accuracy 5 ppm).

The diagnostic peaks, recovered from the first HPLC/UV separation, have been chromatographed by using the two consecutive LC/MS methods (as reported in Section 2) to investigate the possible *o*-toluidine photo-degradation mechanism through the evaluation of reaction intermediates. Representative extracted [M+H]⁺ ion chromatograms, recorded after 3 h of photocatalysis, are reported in Fig. 3 in the case of Z.comm. The peak at 1.1 min is the front of the solvent and it has been recognized by calculating the flow of the HPLC pumping unit. *o*-Toluidine is characterized by a retention time of 4.8 min as confirmed by the extracted ion chromatogram, [M+H]⁺ = 108 *m/z*, reported in Fig. 3a. Three intermediates were identified: 2-hydroxybenzaldehyde (OH-BzH, *m/z* 123, Fig. 3b), *o*-nitrotoluene (NO₂-Tol, *m/z* 138, Fig. 3c), and *o*-methylphenol (CH₃-Ph, *m/z* 109, traces, see Table 2). Table 2 reports the relative abundance of the different intermediates with the reaction evolution (3 and 6 h) for all the tested

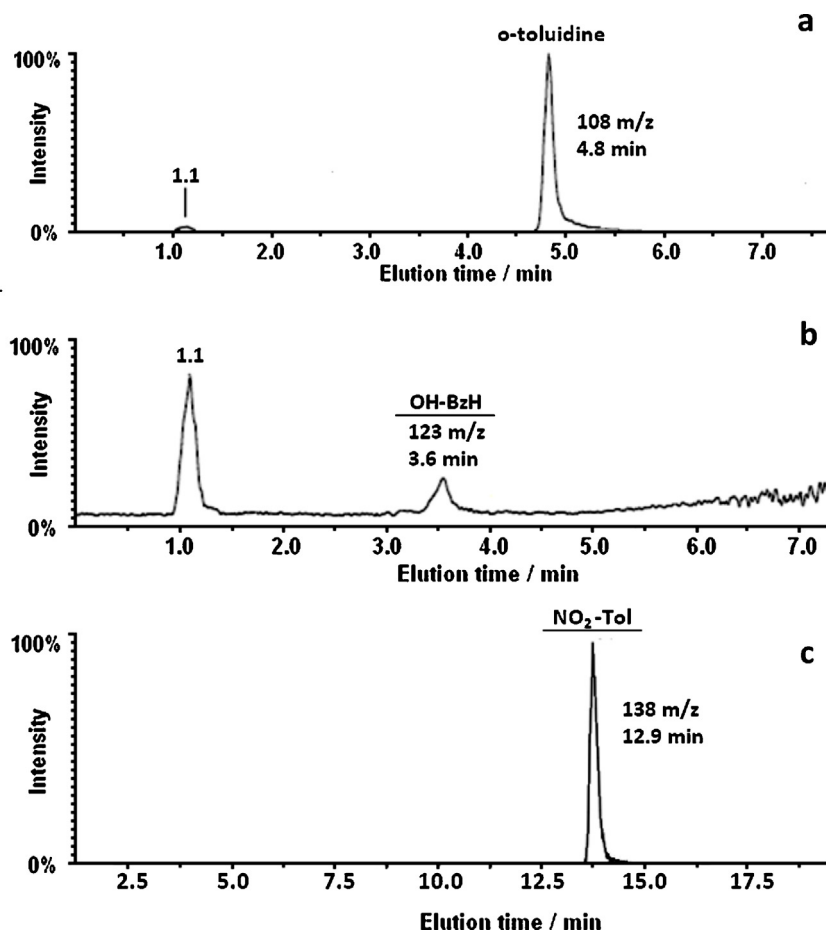


Fig. 3. Extracted [M+H]⁺ ion chromatograms for Z.comm sample: (a) *o*-toluidine, 108 *m/z*; (b) 2-hydroxybenzaldehyde (OH-BzH), 123 *m/z*; (c) *o*-nitrotoluene (NO₂-Tol), 138 *m/z* (Nano-ESI/FTMS).

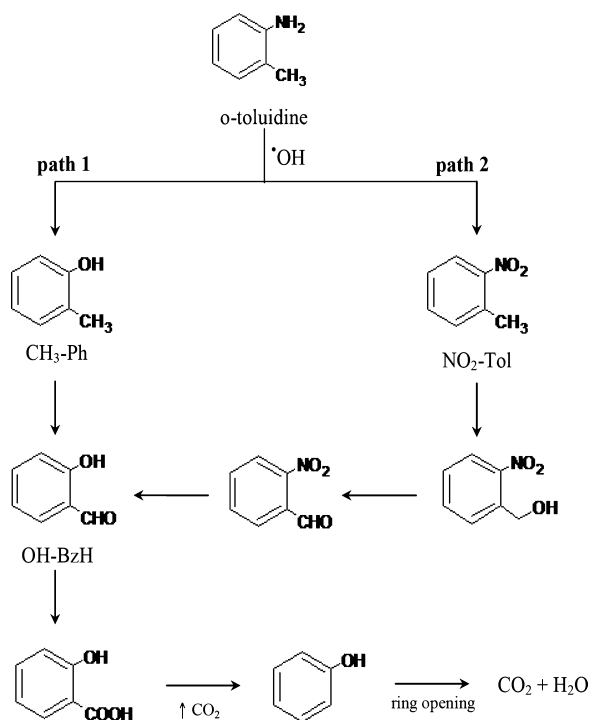


Fig. 4. Proposed photocatalytic degradation pathways for *o*-toluidine in liquid phase.

photocatalysts. The CH₃-Ph degradation product appears only in the case of Z_comm nanopowders. Thus, on the basis of the identified intermediates, a possible photocatalytic degradation mechanism of *o*-toluidine is proposed in Fig. 4. Two different paths might take place simultaneously in agreement with previous reports relative to other photocatalysts [23]. Following pathway 1, *o*-toluidine can be oxidized to *o*-methylphenol by attack of •OH radicals with the elimination of NO₂ group; successively, direct hydrogen abstraction by photohole from the methyl group leads to benzyl radical, followed by the formation of 2-hydroxybenzenemethanol and then 2-hydroxybenzaldehyde (OH-BzH). Instead, in pathway 2, the photocatalytic oxidation of aromatic amino-compounds occurs at the surface of the photocatalyst, as observed by Kamat *et al.* [32] and Fox *et al.* [33] for the photo-degradation of other nitro-compounds in the presence of TiO₂. If the amino group is oxidized to a nitro moiety, this step can be viewed as a 6-electron reaction [32,34]. At this moment, the same hydrogen abstraction occurs leading to 2-nitrobenzaldehyde and further oxidized to 2-hydroxybenzaldehyde (OH-BzH), because the NO₂ group can be easily removed [35]. Finally, for both paths, this stable compound can be partially oxidized to 2-hydroxybenzoic acid, which can convert into phenols, followed by ring opening and partial mineralization. By evaluating the kind of intermediates and their relative abundance, it can be suggested that only by adopting the Z_comm sample the two mechanisms happen concurrently. The contemporary occurrence of two independent degradation pathways might contribute to explain the observed higher activity of Z_comm with respect to Z_SG and Z_ME. This result is fully in agreement with the percentage of pollutant disappearance (Fig. 1) and the final mineralization degree (Table 1).

Further, in order to corroborate these evidences, the trace byproducts adsorbed onto the used ZnO powders were also studied by ATR spectroscopy (Fig. 5). The peaks at around 1260 cm⁻¹ (relative to N–H bending out of plane [36]), at 1200 cm⁻¹ (relative to CH–CH₃ bending [36]), and at 1580–1640 cm⁻¹ (C=C stretching vibration of the aromatic ring [37]) can be ascribable to the

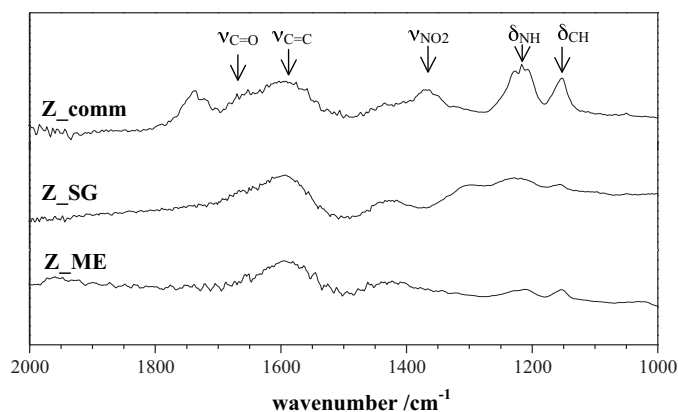


Fig. 5. ATR-FTIR spectra of used ZnO samples.

presence of virgin *o*-toluidine pollutant adsorbed at the photocatalyst surface. Furthermore, intermediate compounds are also adsorbed at the surface of the photocatalyst: (i) the weak band around 1680–1720 cm⁻¹ can be attributed to the presence of aromatic rings with hydroxyl groups as benzoic acid and benzaldehyde (C=O stretching vibration [31,38]); (ii) the band at 1450 cm⁻¹ can be attributed to benzyl alcohol [31]; (iii) the peak at 1350 cm⁻¹ was assigned to the stretching vibration of NO₂ group [39]. By comparing the three spectra of the different ZnO powders, it is worth noting that the Z_comm sample clearly shows the pronounced presence of both the pollutant and the main intermediates in contrast to the laboratory-made samples, as confirmed by LC/MS results.

Indeed, the role of the oxide surface texture and its relative affinity to the pollutant/intermediates in affecting the *o*-toluidine degradation mechanism has to be studied minutely. In the following section, several physicochemical analyses of the studied photocatalysts will be presented to explain potentially the different catalyst behavior regarding the photocatalytic *o*-toluidine removal.

3.2. ZnO powder characterizations

All the ZnO nanopowders, both commercial (Z_comm) and laboratory-made (Z_SG and Z_ME), were finely characterized from morphological (N₂ adsorption isotherm, electron microscopy), optical (diffuse reflectance spectra), and structural (X-ray diffraction) point of views.

The surface area values and the total pore volume of the selected samples were found to be in the range 9–22 m² g⁻¹ (Table 3, 2nd column) and 0.04–0.14 mL g⁻¹ (Fig. S4), respectively. Z_SG sample, obtained by the sol-gel synthetic route, shows the highest surface area, while the sample prepared by the microemulsion (Z_ME) procedure the lowest one, notwithstanding the presence of mesopores (Fig. S4). The hysteresis loop (H3 type) of N₂ isotherms (Fig. S3) is typical of slit-shaped pores for all the samples.

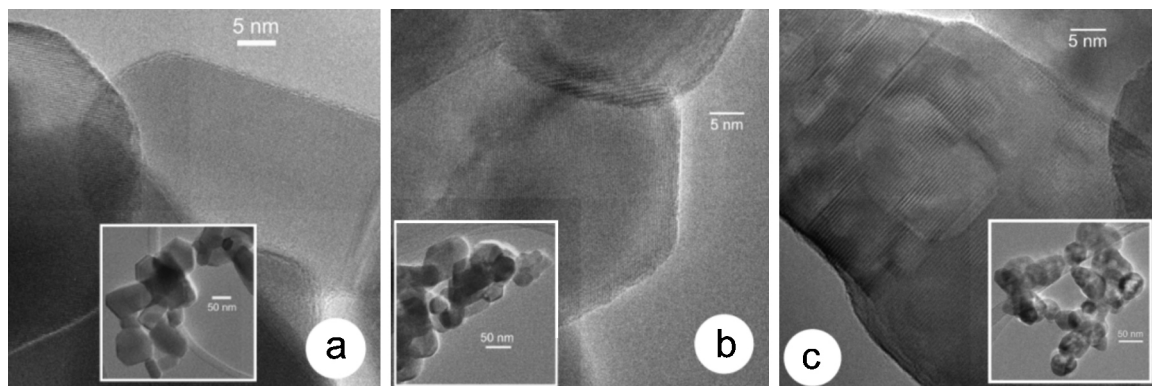
HRTEM images of Z_comm (Fig. 6a) show high crystalline and ordered ZnO nanocrystals with a pseudo-hexagonal shape with an average size of 50 nm (Table 3, 3rd column). Both homemade samples (Z_SG and Z_ME) are characterized by regular ZnO particles (Fig. 6b and c) and the relative interference fringes are ascribable to the 101 planes of wurtzite. The average dimension of the particles for Z_SG and Z_ME is 50 and 20 nm (Table 3), respectively. However, Z_SG particles are characterized by the presence of surface defects, while Z_ME powders show a higher crystallinity degree and a pseudo-hexagonal shape.

All X-ray diffraction peaks can be indexed to hexagonal wurtzite structural ZnO (Fig. S5) and match well with standard hexagonal ZnO (*a* = 3.249 Å and *c* = 5.205 Å, JCPDS Card No. 005-0664), in agreement with HRTEM analyses. No impurity peaks were detected,

Table 3

Surface area, particles/aggregates size, band gap, and recombination time for each adopted sample.

Sample	S_{BET} (m ² g ⁻¹)	$\langle d \rangle^{\text{TEM}}$ (nm)	$\langle d \rangle^{\text{GRAN}}$ (nm)	Band gap (eV)	τ (s)
Z.comm	12	50	100 ± 20 (15%) 300 ± 50 (85%)	3.14	4.1 ± 0.8
Z.SG	22	50	200 ± 50 (20%) 600 ± 100 (80%)	3.05	2.1 ± 0.3
Z.ME	9	20	500 ± 100 (25%) 3000 ± 400 (75%)	3.10	3.0 ± 0.4

**Fig. 6.** HRTEM images of (a) Z.comm, (b) Z.ME, and (c) Z.SG.

indicating the formation of pure products. The sharp and narrow diffraction peaks (Fig. S5) reveal that all the nanopowders are highly crystallized and not extremely small (around 30–70 nm). Then, it is worth noting that when these powders are dispersed in water an increase of aggregation phenomena occurs, leading to big aggregates and limiting the effective photocatalytic active area. Actually for all the tested samples, the distribution of the aggregate size ($\langle d \rangle^{\text{GRAN}}$) by granulometry appears to be bimodal (see Table 3, 4th column) with the main component centered at diameter larger than 300 nm. Among the ZnO samples, a relevant presence of much bigger aggregates (>3000 nm) can be appreciated for Z.ME powders.

Experimental data of diffuse reflectance analysis were converted to absorption coefficient values $F(R)$ according to the Kubelka–Munk relation [31]. Fig. S6 shows the DR curve and the relative transformed reflectance as a function of the photon energy (inset of Fig. S6) of Z.comm, as representative sample. The corresponding band-gap values obtained by this procedure for all samples are reported in Table 3 (5th column). Similar band gap values are appreciable for commercial and laboratory-made samples.

For what concerns the surface characterization obtained by means of FTIR spectroscopy for the various pristine ZnO powders, the main results have been reported in Fig. 7. In the high ν spectral region (Fig. 7a), all samples exhibit (i) a huge (intense and complex) envelope located in the 3600–3100 cm⁻¹ range and (ii) a group of sharp, even if less intense, components located at $\nu > 3600$ cm⁻¹. On the basis of the spectral behavior and of literature data [40], the above-mentioned species can be ascribed to the stretching vibrations of surface OH groups. In particular, the bands located in the 3600–3100 cm⁻¹ range are ascribable to the ν_{OH} of all H-bonded OH groups, including those due to undissociated molecular water (whose spectroscopic δ_{HOH} counterpart lies at ~ 1630 cm⁻¹; see below); on the other hand, all the remaining components (located at $\nu > 3600$ cm⁻¹) can be ascribed to the ν_{OH} of free OH groups present at the surface of the various ZnO materials. This second group of bands becomes more evident after the vacuum thermal treatment carried out at 250 °C, in particular, for the Z.SG material, whereas the huge envelope largely decreases in intensity as a function of the temperature. This is not surprising, as when a surface is set free from most of the species connected to hydration (i.e., either water molecules or weakly bonded OH groups), only

the most strongly held components resist: this is the reason why we can observe the free OH groups only after vacuum activation. Moreover, the Z.SG material retains a larger amount of water in comparing with both Z.comm and Z.ME systems reflecting a more hydrophilic character for the Z.SG sample itself. As for the free OH groups, they are again much better observable for the Z.SG sample, whereas they became negligible for both Z.comm and Z.ME materials: this is again connected to its hydrophilicity. Then, when the low ν spectral region is considered (Fig. 7b), some important features can be put into evidence. A general better definition, along with a parallel much higher intensity, of all the bands is observed for the Z.SG sample in comparison with either Z.comm and Z.ME materials. This is again not surprising, as it reflects the value of specific surface area, which in turn is connected to the possible reactivity of the surface species, at least in part. In fact, sharp and intense bands are evident for the Z.SG material, in particular, in the 1750–1200 cm⁻¹ range: on the basis of their spectral behavior, these components can be ascribed to vibrational modes typical of carbonate-like species [41]. These species may be formed at the surface of oxide materials when the powders are exposed to laboratory atmosphere after the preparation/calcination procedure: the larger the specific surface area, the higher the reactivity of the particles towards water and carbon dioxide contaminant molecules. The possible competition between these adsorbed species and the starting *o*-toluidine pollutant leads to lower degradation capability for the laboratory-made samples (Z.SG and Z.ME) with respect to the commercial one (Z.comm).

Then, the behavior of the samples in inducing different *o*-toluidine removal might also be connected to the recombination rate between the electrons and holes. So, photocurrent–time response of the present ZnO semiconductors was investigated under a constant potential using hand-chopped light. The typical chronoamperometric output of the experiment is shown in Fig. S7 in the case of Z.comm material. The decay observed for all the tested materials indicates that electron–hole recombination processes are occurring, due only to surface recombination as reported in the literature [42,43]. The photocurrent transient can be evaluated by considering the following first-order kinetic equation (inset of Fig. S7) for the first 15 s of decay [24,42]:

$$I(t) = A e^{-t/\tau} + I_f$$

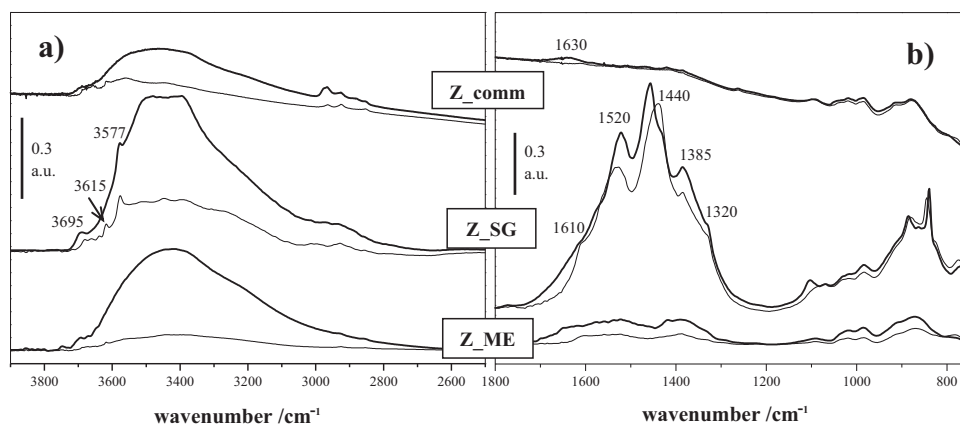


Fig. 7. FTIR spectra of bare ZnO samples: (a) high (3800–2600 cm^{-1}) and (b) low (1800–800 cm^{-1}) ν spectral regions.

where A is a constant, $I(t)$ is the current normalized by both the stationary and the dark values, I_f the current after 15 s, and τ is the transient time constant, related to the mechanism of electron transport. The latter gives indications about the time for charge recombination processes in the semiconductor film. The transient time constant (τ) values, reported in Table 3 (6th column) for the adopted samples, are larger (2–4 s) than those observed by compact single-crystal or polycrystalline electrodes (few milliseconds [42]), but comparable with what reported by other authors in the case oxide photocatalysts [42,44]. It is worth noting that τ for the Z.comm (Table 3, 6th column) is slightly better than those of the laboratory-made ones (especially with respect to the Z.SG) leading to a better charge separation efficiency, confirming the photocatalytic results.

4. Conclusions

In summary, the present research work underlines the pivotal role of surface and bulk properties of ZnO photocatalysts towards the degradation/mineralization of a highly toxic water pollutant, *o*-toluidine. Different photocatalytic responses were observed by using commercial and homemade nanopowders, the latter synthesized by following traditional (sol–gel) and innovative (microemulsion) preparative routes. The best performance was achieved by the commercial Z.comm sample (83% degradation and 26% mineralization) after 6 h of photocatalysis. Several factors are invoked to explain this behavior on the grounds of extensive material characterizations: the lower aggregate size, the higher e^-/h^+ recombination time constant and the availability of surface sites of the pristine sample. Instead, the extremely high surface reactivity of the laboratory-made powders provokes the adsorption of water and carbonate molecules that clogs the surface limiting the interaction between the oxides and the *o*-toluidine molecule. Actually for Z.SG sample the kinetic constant relative to the first 90 min reaction time is the lowest and the degradation trend (over all the 6 h of photocatalysis) does not reach a plateau value justifying the concomitant adsorption/desorption of both *o*-toluidine/intermediates and undesired ambient species.

These evidences are also confirmed by the evaluation of the photocatalytic degradation pathways by LC/MS analyses. The Z.comm sample is the only one that follows two different paths; it is characterized by faster degradation rate and lower presence of byproducts. However, for all the samples, the final mineralization is not significant, probably due to the formation of highly stable OH-BzH intermediates. Moreover, ATR results of the used powders show that for Z.comm both the initial pollutant and the main intermediates are mainly adsorbed onto the surface of

the catalyst in contrast to what occurs with the laboratory made ones.

Finally, selected tests were performed under solar irradiation in the case of the most active sample, Z.comm; despite the decrease in the final activity, these results are very promising, especially when a dopant species will be introduced in the ZnO matrix with the aim to enhance the absorption in the visible region.

Appendix A. Supplementary data

Supplementary data associated with this article can be found, in the online version, at <http://dx.doi.org/10.1016/j.apcatb.2014.08.043>.

References

- [1] R. Stabbert, K.-H. Schäfer, C. Biefel, K. Rustemeier, *Rapid Commun. Mass Spectrom.* 17 (2003) 2125.
- [2] T. Carreón, M.J. Hein, K.W. Hanley, S.M. Viet, A.M. Ruder, *Occup. Environ. Med.* 71 (2014) 175.
- [3] E. Richter, K. Gaber, U.A. Harréus, C. Matthias, N. Kleinsasser, *Toxicol. Lett.* 164 (2006) S255.
- [4] G. Korin, L. Lüersen, K.H. Schaller, J. Angerer, H. Drexler, *Toxicol. In Vitro* 22 (2008) 812.
- [5] L. Falcicola, V. Pifferi, E. Mascheroni, *Electroanalysis* 24 (2012) 767.
- [6] J. Anotai, P. Thupitmdang, C.-C. Su, M.-C. Lu, *Environ. Sci. Pollut. Res. Int.* 19 (2012) 169.
- [7] J. Anotai, S. Singhadech, C.-C. Su, M.-C. Lu, *J. Hazard. Mater.* 196 (2011) 395.
- [8] N. Masomboon, C.-W. Chen, J. Anotai, M.-C. Lu, *Chem. Eng. J.* 159 (2010) 116.
- [9] T. An, L. Sun, G. Li, S. Wan, *J. Mol. Catal. A Chem.* 333 (2010) 128.
- [10] P. Bansal, D. Sud, *Sep. Purif. Technol.* 85 (2012) 112.
- [11] N. Daneshvar, M.H. Rasoulifard, A.R. Khataee, F. Hosseinzadeh, *J. Hazard. Mater.* 143 (2007) 95.
- [12] J.O. Saucedo-Lucero, S. Arriaga, *Chem. Eng. J.* 218 (2013) 358.
- [13] H. Tong, S. Ouyang, Y. Bi, N. Umezawa, M. Oshikiri, J. Ye, *Adv. Mater.* 24 (2012) 229.
- [14] R. Ianoş, I. Lazău, C. Păcurariu, P. Sfîrloagă, *Mater. Chem. Phys.* 129 (2011) 881.
- [15] M.-H. Wang, X.-Y. Ma, W. Jiang, F. Zhou, *Mater. Lett.* 121 (2014) 149.
- [16] S. López-Cuenca, L.A. Pérez Carrillo, M. Rabelero Velasco, R. Díaz de León, H. Saade, R.G. López, E. Mendizábal, J.E. Puig, *J. Nanomater.* 2011 (2011) 1.
- [17] F.B. Dejene, A.G. Ali, H.C. Swart, R.J. Botha, K. Roro, L. Coetsee, M.M. Biggs, *Cent. Eur. J. Phys.* 9 (2011) 1321.
- [18] J. Eastoe, B. Warne, *Curr. Opin. Colloid Interf. Sci.* 1 (1996) 800.
- [19] M.P. Pileni, *Langmuir* 17 (2001) 7476.
- [20] J. Tanori, M.P. Pileni, *Langmuir* 13 (1997) 639.
- [21] J.-C. Lin, C.-P. Lee, K.-C. Ho, *J. Mater. Chem.* 22 (2012) 1270.
- [22] R.L. Gupta, I.P. Kaur, A.K. Gupta, D.P. Pathak, T.R. Juneja, *Toxicol. Lett.* 48 (1989) 75.
- [23] T. An, L. Sun, G. Li, S. Wan, *J. Mol. Catal. A Chem.* 333 (2010) 128.
- [24] F. Spadavecchia, S. Ardizzone, G. Cappelletti, L. Falcicola, M. Ceotto, D. Lotti, *J. Appl. Electrochem.* 43 (2012) 217.
- [25] X. Wang, S. Liu, Q. Xia, G. Zhao, J. Guo, F. Xie, *J. Sep. Sci.* 36 (2013) 3750.
- [26] E.M. Sheldon, *J. Pharm. Biomed. Anal.* 31 (2003) 1153.
- [27] X. Li, D.R. Ballerini, W. Shen, *Biomicrofluidics* 6 (2012) 11301.
- [28] C. Fanali, L. Dugo, P. Dugo, L. Mondello, *Trends Anal. Chem.* 52 (2013) 226.
- [29] M. Ceotto, L. Lo Presti, G. Cappelletti, D. Meroni, F. Spadavecchia, R. Zecca, M. Leoni, P. Scardi, C.L. Bianchi, S. Ardizzone, *J. Phys. Chem. C* 116 (2012) 1764.

- [30] L. Lo Presti, M. Ceotto, F. Spadavecchia, G. Cappelletti, D. Meroni, R.G. Acres, S. Ardizzone, *J. Phys. Chem. C* 118 (2014) 4797.
- [31] D. Meroni, S. Ardizzone, G. Cappelletti, C. Oliva, M. Ceotto, D. Poelman, H. Poelman, *Catal. Today* 161 (2011) 169.
- [32] P.V. Kamat, *Chem. Rev.* 93 (1993) 267.
- [33] M.A. Fox, M.T. Dulay, *Chem. Rev.* 93 (1993) 341.
- [34] S. Chen, H. Zhang, X. Yu, W. Liu, *Chin. J. Chem.* 28 (2010) 21.
- [35] W. Zhang, X. Xiao, T. An, Z. Song, J. Fu, G. Sheng, M. Cui, *J. Chem. Technol. Biotechnol.* 78 (2003) 788.
- [36] E.M. Andrade, F.V. Molina, M. Florit, D. Posadas, *J. Electroanal. Chem.* 415 (1996) 153.
- [37] B. Pal, M. Sharon, *J. Mol. Catal. A Chem.* 160 (2000) 453.
- [38] L. Cao, *J. Catal.* 196 (2000) 253.
- [39] F. Frola, F. Prinetto, G. Ghiotti, L. Castoldi, I. Nova, L. Lietti, P. Forzatti, *Catal. Today* 126 (2007) 81.
- [40] H. Noei, H. Qiu, Y. Wang, E. Löffler, C. Wöll, M. Muhler, *Phys. Chem. Chem. Phys.* 10 (2008) 7092.
- [41] G. Busca, V. Lorenzelli, *Mater. Chem.* 7 (1982) 89.
- [42] R. Dholam, N. Patel, A. Santini, A. Miotello, *Int. J. Hydrogen Energy* 35 (2010) 9581.
- [43] D. Tafalla, *J. Electrochem. Soc.* 137 (1990) 1810.
- [44] D. Meroni, V. Pifferi, B. Sironi, G. Cappelletti, L. Falciola, G. Cerrato, S. Ardizzone, *J. Nanoparticle Res.* 14 (2012) 1086.